

negative regulators of apoptosis such as Bcl-2 (8, 9) and IAPs (10) have been shown to have oncogenic activities as well. The inhibition of apoptosome formation by ProT also offered an explanation for a long-standing puzzling observation that up to a millimolar concentration of dATP is required to trigger efficient caspase-3 activation in vitro. The intracellular dATP under normal conditions is in the 10- μ M range and does not arise during apoptosis (36). The requirement for millimolar dATP also contradicts the direct binding studies with purified Apaf-1 and dATP. In this study, the dissociation constant of dATP binding to Apaf-1 is at the micromolar level in the presence of cytochrome c, and micromolar amounts of dATP also efficiently stimulate caspase-3 activation in a reconstituted system containing purified Apaf-1, procaspase-9, and cytochrome c (3). It is clear now that most dATP is probably used for repressing ProT in HeLa cell S-100. When ProT is suppressed by PETCM, 10 μ M dATP is enough to trigger apoptosome formation and PHAP can subsequently accelerate the activity of the machinery. Unlike ProT, PHAP proteins function as tumor suppressors in mammalian cells to inhibit cell growth (21, 25, 26). They have been shown to inhibit protein phosphatase 2A (37) and block histone acetylase (38). How these biochemical functions are linked to its cellular antigrowth function is not clear. But, in light of our finding that PHAP proteins promote apoptosis by accelerating

caspase-9 activation, we suggest that it may inhibit cell growth by promoting apoptosis. Interestingly, PHAP can interact with ataxin-1, a protein that is mutated in the neural degenerative disease spinocerebellar ataxia type 1 (22). This suggests a role of PHAP in the disease. Further, certain PHAP proteins are preferentially expressed in mouse cerebellum during its most active developmental period characterized by massive apoptosis (39–41). Because apoptosis and Apaf-1 are essential in this early brain developmental stage (42, 43), we suggest that PHAP, a stimulator of apoptosome activity, might also play a crucial role during brain development, a readily testable model.

References and Notes

1. J. C. Goldstein *et al.*, *Nature Cell Biol.* **2**, 15 (2000).
2. X. Wang, *Genes Dev.* **15**, 2922 (2001).
3. X. Jiang, X. Wang, *J. Biol. Chem.* **275**, 31199 (2000).
4. D. Acehan *et al.*, *Mol. Cell* **9**, 423 (2002).
5. P. Li *et al.*, *Cell* **91**, 479 (1997).
6. J. Rodriguez, Y. Lazebnik, *Genes Dev.* **13**, 3179 (1999).
7. N. A. Thornberry, Y. Lazebnik, *Science* **281**, 1312 (1998).
8. J. M. Adams, S. Cory, *Science* **281**, 1322 (1998).
9. D. T. Chao, S. J. Korsmeyer, *Annu. Rev. Immunol.* **16**, 395 (1998).
10. Q. L. Deveraux, J. C. Reed, *Genes Dev.* **13**, 239 (1999).
11. C. Du *et al.*, *Cell* **102**, 33 (2000).
12. A. M. Verhagen *et al.*, *Cell* **102**, 43 (2000).
13. A. M. Verhagen *et al.*, *J. Biol. Chem.* **277**, 445 (2001).
14. Y. Suzuki *et al.*, *Mol. Cell* **8**, 613 (2001).
15. R. Hegde *et al.*, *J. Biol. Chem.* **277**, 432 (2001).
16. X. Liu *et al.*, *Cell* **86**, 147 (1996).
17. X. Jiang *et al.*, data not shown.
18. See supporting data on Science Online.
19. H. Zou *et al.*, *Cell* **90**, 405 (1997).

20. M. Vaesen *et al.*, *Biol. Chem. Hoppe-Seyler* **375**, 113 (1994).
21. T. H. Chen *et al.*, *Mol. Biol. Cell* **7**, 2045 (1996).
22. A. Matilla *et al.*, *Nature* **389**, 974 (1997).
23. L. Zhu *et al.*, *Biochem. Mol. Biol. Int.* **42**, 927 (1997).
24. M. Mencinger *et al.*, *Biochim. Biophys. Acta* **1395**, 176 (1998).
25. J. R. Brody *et al.*, *J. Biol. Chem.* **274**, 20053 (1999).
26. J. Bai *et al.*, *Oncogene* **20**, 2153 (2001).
27. M. Dosit *et al.*, *Exp. Cell Res.* **204**, 94 (1993).
28. R. S. Orre *et al.*, *J. Biol. Chem.* **276**, 1794 (2001).
29. A. Pineiro *et al.*, *Peptides* **21**, 1433 (2000).
30. A. R. Sbrulati *et al.*, *Proc. Natl. Acad. Sci. U.S.A.* **88**, 253 (1991).
31. M. R. Smith *et al.*, *Blood* **82**, 1127 (1993).
32. P. Rodriguez *et al.*, *Biochem. J.* **331**, 753 (1998).
33. C. Magdalena *et al.*, *Br. J. Cancer* **82**, 584 (2000).
34. C. G. Wu *et al.*, *Br. J. Cancer* **76**, 1199 (1997).
35. M. Eilers *et al.*, *EMBO J.* **10**, 133 (1991).
36. P. W. Mesner Jr. *et al.*, *J. Biol. Chem.* **274**, 22635 (1999).
37. M. Li, A. Makkinje, Z. Damuni, *Biochemistry* **35**, 6998 (1996).
38. S. B. Seo *et al.*, *Cell* **104**, 119 (2001).
39. K. Matsuoka *et al.*, *Proc. Natl. Acad. Sci. U.S.A.* **91**, 9670 (1994).
40. H. Mutai *et al.*, *Biochem. Biophys. Res. Commun.* **274**, 427 (2000).
41. M. Radrizzani, *J. Brain Res.* **907**, 162 (2001).
42. F. Ceconi *et al.*, *Cell* **94**, 727 (1998).
43. H. Yoshida *et al.*, *Cell* **94**, 739 (1998).
44. We thank F. Du and R. Harold for excellent technical support and Q. Liu for critical reading of the manuscript. Supported by the Howard Hughes Medical Institute, NIH grant GMRO1-57158, and Welch Foundation grant I-1412.

Supporting Online Material

www.sciencemag.org/cgi/content/full/299/5604/223/DC1
Materials and Methods
Fig. S1

31 July 2002; accepted 29 October 2002

REPORTS

Nanoparticle Assembly and Transport at Liquid-Liquid Interfaces

Y. Lin,¹ H. Skaff,¹ T. Emrick,^{1*} A. D. Dinsmore,^{2*} T. P. Russell^{1*}

The self-assembly of particles at fluid interfaces, driven by the reduction in interfacial energy, is well established. However, for nanoscopic particles, thermal fluctuations compete with interfacial energy and give rise to a particle-size-dependent self-assembly. Ligand-stabilized nanoparticles assembled into three-dimensional constructs at fluid-fluid interfaces, where the properties unique to the nanoparticles were preserved. The small size of the nanoparticles led to a weak confinement of the nanoparticles at the fluid interface that opens avenues to size-selective particle assembly, two-dimensional phase behavior, and functionalization. Fluid interfaces afford a rapid approach to equilibrium and easy access to nanoparticles for subsequent modification. A photoinduced transformation is described in which nanoparticles, initially soluble only in toluene, were transported across an interface into water and were dispersed in the water phase. The characteristic fluorescence emission of the nanoparticles provided a direct probe of their spatial distribution.

Directed self-assembly of nanoparticles opens new avenues of technology through the controlled fabrication of nanoscopic materials

with unique optical, magnetic, and electronic properties (1–5). Ligand-stabilized colloidal nanoparticles are ideally suited to hierarchi-

cal self-assembly, because the nanoparticle core dictates optical, electronic, or magnetic properties, whereas the surface-bound ligands define the particle's interactions with its surroundings. A fluid-fluid interface offers potential for such assembly (6, 7) and for the chemical manipulation of nanoparticles. At a fluid interface, the particles are highly mobile and rapidly achieve an equilibrium assembly. The rapid diffusion of nanoparticles and reagents in either fluid also leads to very efficient interfacial chemistry. Surfaces of dispersed droplets offer a substantially greater interfacial area than a planar interface. Moreover, the size and shape of droplets can be controlled from microscopic to macroscopic

¹Department of Polymer Science and Engineering,

²Department of Physics, University of Massachusetts, Amherst, MA 01003, USA.

*To whom correspondence should be addressed. E-mail: tsemrick@mail.pse.umass.edu (T.E.); dinsmore@physics.umass.edu (A.D.D.); russell@mail.pse.umass.edu (T.P.R.)

dimensions by use of an external force. Interfaces between immiscible fluids, on the surface of droplets, have been shown to be ideal for the assembly of micrometer-sized colloidal particles (8). The interfacial segregation of particles is well-established in froth flotation processes for the extraction of precious mineral ore from the gangue before smelting (9). For nanoparticles, however, thermal energy, which causes spatial fluctuations of the particles, is comparable to the interfacial energy. This energy balance results in a weak interfacial segregation of nanoparticles. Here, we show that size-dependent adsorption and desorption of nanoparticles from an interface occurred and gave rise to a two-dimensional phase separation at the interface. Moreover, the fluid-fluid interfaces provided easy access to the nanoparticles for their chemical modification by the reaction of attached ligands with reagents in both fluids. In particular, tri-*n*-octylphosphine oxide (TOPO)-covered cadmium selenide (CdSe) nanoparticles dispersed in toluene organized at the interfaces of water droplets and underwent a photoinduced ligand transformation in which the nanoparticles were transported across the interface and were dispersed in water.

TOPO-covered CdSe nanoparticles were prepared by methods described in the literature (10, 11). Repeated precipitation of the nanoparticles in methanol removed most of the TOPO not bound to the nanoparticle surface, leading to a core-shell nanoparticle-TOPO structure. With this TOPO coverage, the CdSe nanoparticles could be dispersed in toluene and other organic solvents. Confocal microscopy studies were performed on a Leica TCS SP2 laser confocal scanning microscope (LCSM).

Figure 1A shows a $\sim 20\text{-}\mu\text{m}$ -diameter water droplet dispersed in toluene containing 2.8-nm-diameter CdSe nanoparticles. The images show the fluorescence from the nanoparticles (excitation, 488 nm; emission, 525 nm). Each image is an optical cross-section taken at 2.7- μm intervals in depth through the droplet. Together, these data show that the droplet was spherical and that the nanoparticles segregated to the toluene-water interface, stabilizing the droplet. The droplets were stable against coalescence for days. Detailed reflection interference contrast microscopy studies (12, 13) on dispersed droplets, coupled with atomic force and electron microscopy studies on dried droplets, showed that the nanoparticles formed a monolayer at the interface. X-ray scattering and electron microscopy studies on dried droplets showed that the arrangement of the particles on the surface was liquid-like, with no long-range order and an average separation distance between the particles commensurate with the diameter of the nanoparticles plus twice the

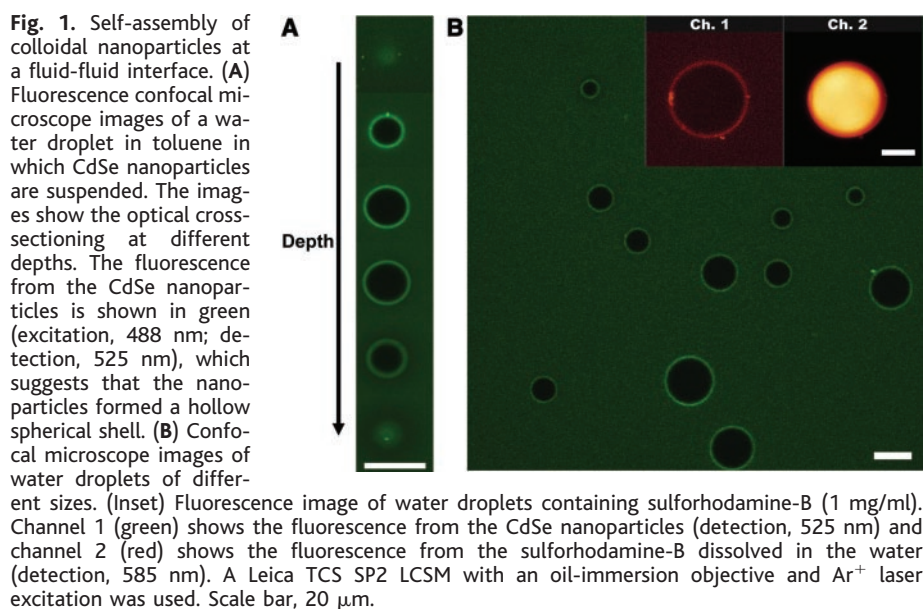
length of the stabilizing ligand. Fluorescence photobleaching (14, 15) studies on the suspended droplets showed that the nanoparticles were mobile and laterally diffused over the surface of the droplet. Nanoparticle-coated water droplets with diameters from 10 to 100 μm were obtained by the addition of water to a dispersion of the nanoparticles in toluene, followed by shaking; smaller droplet diameters can be obtained by sonication. No efforts were made to control the average size or polydispersity of the droplets (Fig. 1B). Shown in the inset of Fig. 1B is the fluorescence image of a similar sample in which a fluorescent dye, sulforhodamine-B, was initially dissolved in the water. We examined the CdSe nanoparticles and sulforhodamine-B independently by observing their fluorescence at 525 and 585 nm, respectively. The nanoparticles segregated to the toluene-water interface, and the sulforhodamine-B, dissolved in the water phase, was fully encapsulated by the nanoparticles. No evidence of CdSe in the water phase or sulforhodamine-B in the toluene phase was observed, as would be expected from the hydrophobic nature of the TOPO-covered nanoparticles and the hydrophilic nature of sulforhodamine-B.

Interfacial assembly of nanoparticles is dictated by a minimization of the Helmholtz free energy. Placement of one nanoparticle at an interface will decrease the entropy by about k_B (the Boltzmann constant). Consequently, the energy change, ΔE , must be negative to reduce the total free energy. The three contributions to the interfacial energy arise from the particle-oil interface ($\gamma_{P/O}$), the particle-water interface ($\gamma_{P/W}$), and the oil-water interface ($\gamma_{O/W}$). ΔE , due to the assembly of a single particle at the oil-water interface, is given by

$$\Delta E = -\frac{\pi R^2}{\gamma_{O/W}} \times [\gamma_{O/W} - (\gamma_{P/W} - \gamma_{P/O})^2]$$

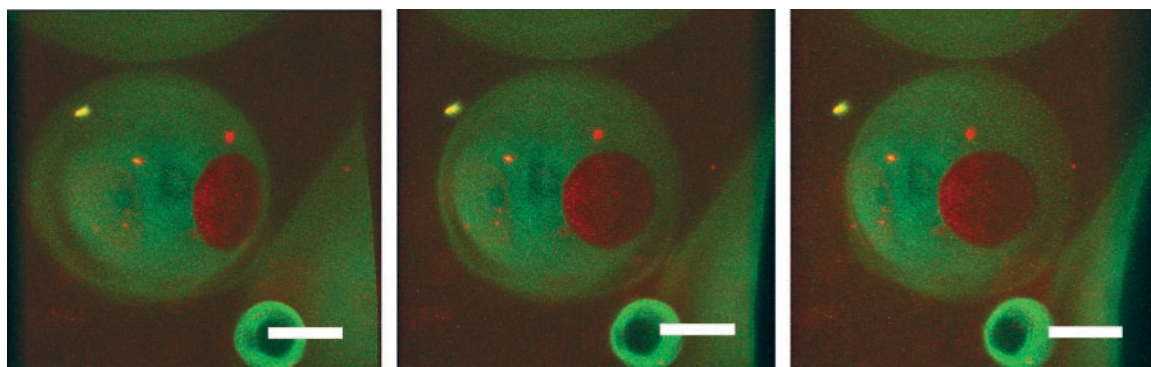
(6, 16), where R is the effective radius of the nanoparticle. On the basis of published values (17) for $\gamma_{O/W}$ of 35.7 mN/m and on estimates for $\gamma_{P/O}$ of ~ 15 mN/m and for $\gamma_{P/W}$ of ~ 40 mN/m, ΔE is about $-5 k_B T$ for 2.8-nm-diameter nanoparticles, where T is absolute temperature. Because ΔE depends on R^2 , the energy gain is smaller and the assembly is less stable for smaller nanoparticles than for larger ones. Consequently, thermal energy is sufficient to induce a displacement of the particles from the interface. In fact, no droplet stabilization was observed when particles with diameters less than ~ 1.6 nm were used.

The weak energy associated with the assembly of the nanoparticles at the interface gives rise to a thermally activated escape. The residence time of the nanoparticle at the interface increases with increasing particle size. Thus, unlike larger, micrometer-sized particles that are strongly held at the interface, it is possible for smaller nanoparticles at an interface to be preferentially displaced with the larger ones. We introduced 4.6-nm particles in toluene to a dispersion containing water droplets in toluene that had been stabilized with 2.8-nm particles (Fig. 2). The 2.8-nm particles, which fluoresce at 525 nm, are shown as green, whereas the 4.6-nm particles, which fluoresce at 610 nm, are red. The 4.6-nm particles assembled on the surface of an existing stabilized droplet, displacing the smaller 2.8-nm particles. The spontaneous escape of the 2.8-nm nanoparticles is consistent with a ΔE of about $-5 k_B T$. Displacement of larger nanoparticles with smaller nanoparticles did not occur, in keeping with the arguments above. This simple displacement



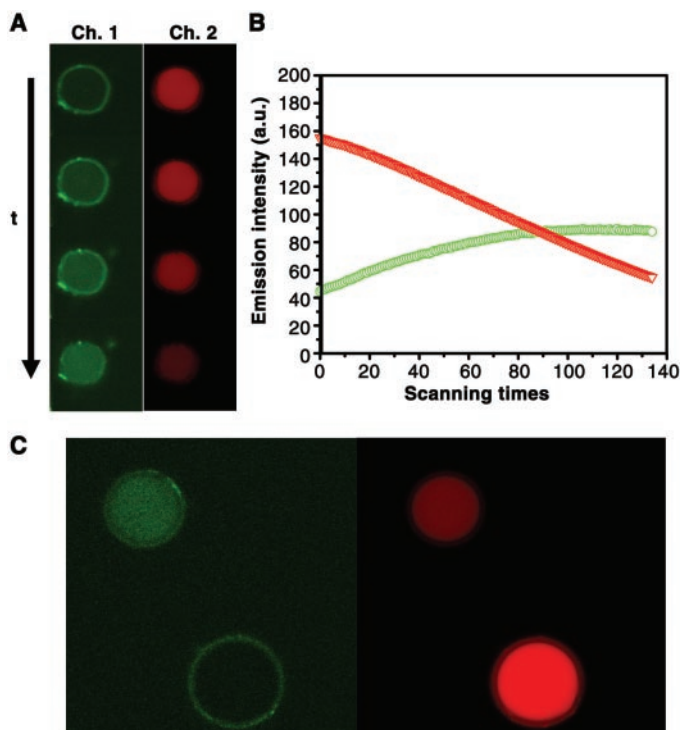
REPORTS

Fig. 2. Three-dimensional reconstructions of confocal microscopic images of a dispersion of water droplets stabilized by 2.8-nm-diameter CdSe nanoparticles (green) after the introduction of a solution of 4.6-nm-diameter CdSe nanoparticles (red). The three images are the same volume of the sample rotated in the field of view. As seen, the 4.6-nm nanoparticles



displace the 2.8-nm nanoparticles and show evidence of a phase separation on the water droplet surface. Scale bar, 16 μm .

Fig. 3. The hydrophobic-to-hydrophilic conversion of stabilized nanoparticles. (A) A water droplet in toluene observed with a confocal fluorescence microscope with 488-nm excitation. Channel 1 (green, left side) shows the nanoparticle fluorescence (detection, 525 nm) over a period of several minutes during continuous illumination with 488-nm light. Channel 2 (red, right side) shows the fluorescence from the sulforhodamine-B dissolved in the water (detection, 585 nm). Over a period of several minutes, the nanoparticles spontaneously accumulated inside the aqueous droplet. *t*, time. (B) The average fluorescence intensity inside the water droplet versus scanning times. Green circles show data from channel 1; red triangles show data from channel 2. a.u., arbitrary units. (C) The droplet irradiated with 488-nm light (top left droplet) is compared with the nearby droplet (lower left) without irradiation. Images on the right are the fluorescence images at 585 nm of the same droplets. Scale bar, 10 μm .



process is unique to nanoparticles, in which thermal fluctuations can be dominant. Figure 2 also shows a two-dimensional size-dependent segregation at the interface separating the two fluids, observable by the unique dependence of the fluorescence emission wavelength on the nanoparticle size.

A chemical interaction between the sulforhodamine-B, dissolved in the water, with the nanoparticles at the interface was found after the stabilized water droplets were repeatedly scanned with 488-nm light. The time-dependent cross-sectional image of a dispersed droplet is shown in Fig. 3A. Initially, results identical to those shown in the inset of Fig. 1B were obtained, in which the nanoparticles segregated to the interface. As more energy was placed into the system by repeated scanning, the CdSe nanoparticles crossed

the toluene-water interface and became dispersed in the water phase (Fig. 3A, channel 1). The fluorescence from the sulforhodamine-B was always restricted to within the droplet, but its intensity decreased with time (Fig. 3B). This is shown in Fig. 3C, where two droplets are included within the field of view. The lower droplet was scanned only once, whereas the upper droplet was scanned 140 times. The segregation of the nanoparticles to the interface persisted in the repeatedly scanned droplet, and the water phase was entrapped by the nanoparticle layer. However, fluorescent nanoparticles were also observed within the water phase, i.e., some nanoparticles were transported across the toluene-water interface. In the absence of the sulforhodamine-B, transfer of the nanoparticles across the water-toluene interface did

not occur and the nanoparticles remained excluded from the water phase. Thus, in the presence of the dye and upon extended irradiation, the initially hydrophobic (toluene-soluble) nanoparticles were converted into hydrophilic (water-soluble) particles.

These observations require the in situ formation of a hydrophilic ligand environment around the nanoparticle. We found insight into the reaction mechanism by simultaneously monitoring the fluorescence from the nanoparticles (525 nm) and the dye (585 nm). As shown in Fig. 3B, the former increased within the droplet until it plateaued, whereas the latter, only seen within the droplet, continuously decreased with time. This observation was not due to a shift in the emission spectrum of the sulforhodamine-B after irradiation. The emission spectrum within the droplets was monitored in situ and no significant shift of the characteristic emission band was observed. Control experiments on droplets of water containing the dye did not show significant photobleaching under identical conditions. Because the reduction in the sulforhodamine-B fluorescence occurred only in the presence of the nanoparticles, it can be concluded that interactions between the dye and the nanoparticles enhanced the photobleaching rate of the dye. The specific chemical interactions responsible for the hydrophobic/hydrophilic transformation are not quantitatively understood at present. However, a plausible mechanism would be the adsorption of one of the dye's functional moieties, such as the sulfonate or diethylamine, to the nanoparticle surface. For example, adsorption of dye molecules to the nanoparticle surface via the cationic site on the dye would expose a hydrophilic sulfonate periphery and lead to water solubility. This could occur by negative charging of the nanoparticle surface due to the presence of surfactants on the nanoparticle surface (18). This mechanism is consistent with the surface-induced photo-oxidation pathways reported for sulforhodamine-B on titanium dioxide and cadmium sulfide surfaces (19, 20).

We have shown a simple, robust means of

directing nanoparticle assembly at a fluid-fluid interface. The small particle size gave rise to an interfacial adsorption energy comparable to a few $k_B T$. The spontaneous tendency to replace small nanoparticles with larger nanoparticles at the interface and the patterns formed by size-dependent lateral phase separation open possibilities for forming functionally distinct regions on the droplet surface, a direct route to controlled-release encapsulation and delivery. A photoinduced nanoparticle transport across the toluene-water interface was also demonstrated, in which the solubility of the nanoparticles was changed and their characteristic fluorescence was retained. The ability to easily encapsulate and stabilize water droplets, coupled with

the diversity of ligands that can be placed on the surface of nanoparticles, holds promise for the encapsulation of any water-soluble material with such nanoparticle assemblies.

References and Notes

1. L. Brus, *Appl. Phys. A* **53**, 465 (1991).
2. A. P. Alivisatos, *Science* **271**, 933 (1996).
3. J. Lenglet, A. Bourdon, J. C. Bacri, R. Perzynski, G. Demouchy, *Phys. Rev. B* **53**, 14941 (1996).
4. A. P. Alivisatos *et al.*, *Adv. Mater.* **10**, 1297 (1998).
5. S. A. Empedocles, R. Neuhäuser, M. G. Bawendi, *Nature* **399**, 126 (1999).
6. P. Pieranski, *Phys. Rev. Lett.* **45**, 569 (1980).
7. O. D. Velev, K. Furusawa, K. Nagayama, *Langmuir* **12**, 2374 (1996).
8. A. D. Dinsmore *et al.*, *Science* **298**, 1006 (2002).
9. A. M. Gaudin, *Flotation* (McGraw Hill, New York, 1957).
10. Z. A. Peng, X. G. Peng, *J. Am. Chem. Soc.* **123**, 183 (2001).
11. H. Skaff, M. F. Ilker, E. B. Coughlin, T. Emrick, *J. Am. Chem. Soc.* **124**, 5729 (2002).
12. J. Radler, E. Sackmann, *J. Phys. II Fr.* **3**, 727 (1993).
13. G. Wiegand, K. Neumaier, E. Sackmann, *Appl. Opt.* **37**, 6892 (1998).
14. D. Axelrod, D. E. Koppel, J. Schlessinger, E. Elson, W. W. Webb, *Biophys. J.* **16**, 1055 (1976).
15. J. C. G. Blonk, A. Don, H. V. Aalst, J. J. Birmingham, *J. Microsc.* **169**, 363 (1993).
16. B. P. Binks, J. H. Clint, *Langmuir* **18**, 1270 (2002).
17. K. S. Birdi, D. T. Vu, *Handbook of Surface and Colloid Chemistry* (CRC Press, Boca Raton, FL, 1997).
18. L. Qu, Z. A. Peng, X. G. Peng, *Nano Lett.* **1**, 333 (2001).
19. G. M. Liu, X. Z. Li, J. C. Zhao, H. Hidaka, N. Serpone, *Environ. Sci. Technol.* **34**, 3982 (2000).
20. T. Watanabe, T. Takizawa, K. Honda, *J. Phys. Chem.* **81**, 1845 (1977).
21. Supported by the Department of Energy, Office of Energy Science, and the NSF-supported Materials Research Science and Engineering Center.

20 September 2002; accepted 19 November 2002

Quantum Phase Transition in Organic Charge-Transfer Complexes

Sachio Horiuchi,^{1*} Yoichi Okimoto,¹ Reiji Kumai,¹ Yoshinori Tokura^{1,2,3}

A phase transition in an organic charge-transfer complex, which originates from the neutral-ionic valence instability, can be tuned toward zero kelvin with use of external pressure or chemical modification as a control parameter. The phase diagram and observed dielectric behaviors are typical of quantum paraelectricity, yet this zero-kelvin transition point namely, the quantum critical point, accompanies large quantum fluctuation of the molecular charge, as demonstrated by the molecular vibrational mode spectra. The result indicates that the π -electron transfer between donor and acceptor molecules is coupled with the zero-point lattice dynamics around the quantum critical point.

Charge-transfer interaction between molecules plays a key role in producing electronic, magnetic, and/or optical functionality in organic solids. Typically, the charge-transfer (CT) complexes, composed of π -electron donor (D) and acceptor (A) molecules, carry an electric charge and spin on the respective molecular site, forming molecular metals, superconductors, magnets, ferroelectrics, and so forth (I - A). In some CT complexes that have dominant interaction along the DA alternating stack, the component molecules show a valence instability, termed neutral-ionic (NI) transition (5), when external stimuli, such as temperature change, pressure, current injection, and light-irradiation, are ap-

plied to them in their critical state (4). The primary feature of this valence instability is a change in the π -electron density on the respective molecules that transforms a van der Waals crystal of neutral (N) molecules into an ionic (I) crystal in which the radical spins reside on the respective D and A molecules. The spin-Peierls-like instability that forms the spin-singlet DA pair in the I phase can generate a polar DA stack, such as $D^+A^-D^+A^-D^+A^-$, which endows the NI transition with a ferroelectric nature (6 , 7), and thereby with nonlinear optical activity (8). Here, we describe the valence control that extends the NI transition point toward 0 K, using pressure and chemical composition as control parameters. Such a 0-K transition point, or quantum critical point (QCP), plays an essential role in many quantum phenomena, such as exotic superconductivity and non-Fermi liquid or magnetic instability behaviors of metal, which are ubiquitously observed in the QCP's proximity region (9 - 11). In the present case, the quantum fluctuation of the molecular valence between the energetically degenerate N and I states is manifested as the

quantum paraelectric behavior in the dielectric response, as well as the low activation energy of the charge transport subsisting to low temperature.

One of the external parameters driving the NI transition is volume contraction of the crystal, which modifies the energy balance between the electrostatic Madelung gain and the cost of ionization while increasing the degree of CT ρ (the ionicity defined by $D^{+p}A^{-p}$) (5). For the purpose of tuning the critical condition by chemical modification of constituent molecules, one useful material system is derived from the complex of $D = \text{DMTTF}$ (4,4'-dimethyltetrathiafulvalene) and $A = \text{tetrachloro-}p\text{-benzoquinone}$ (see the molecular structures in Fig. 1), which undergoes the NI transition of second order (or very weak first order) at phase transition temperature $T_c = 65$ K (12). Earlier work has developed isomorphous crystals for a series of Br-substituted tetrahalo- p -benzoquinones [$\text{QBr}_n\text{Cl}_{4-n}$, where n is number of Br atoms ranging from zero to four (Fig. 1)] (13). The Br substitution gives rise to modest lattice expansion, while nearly preserving the electron affinity of the A molecule. Owing to the effectively negative pressure, the I phase vanishes completely upon the full Br substitution ($A = \text{QBr}_4$). The 2,6-dibromo-substituted compound (2,6-QBr₂Cl₂) ($X_1 = X_4 = \text{Cl}$, $X_2 = X_3 = \text{Br}$ in Fig. 1) stands near its vanishing point as the intermediate. The DMTTF-QBr₄ complex is hence an ideal compound, in which the NI transition can be traced entirely from the $T = 0$ point when hydrostatic pressure is applied as the continuous and homogeneous external parameter.

In the temperature dependence of the dielectric constant ϵ for a DMTTF-QBr₄ crystal under various pressures (Fig. 1), ϵ remains small at ambient pressure, as the paraelectric N phase is stable. Below 1 kbar, the ϵ increases upon cooling toward $T = 0$ K, but a lack of the peak anomaly suggests that no phase transition emerges down to $T = 0$. In con-

¹Correlated Electron Research Center (CERC), National Institute of Advanced Industrial Science and Technology (AIST), Tsukuba, 305-8562, Japan. ²Spin Superstructure Project (SSS), ERATO, Japan Science and Technology Corporation (JST), c/o National Institute of Advanced Industrial Science and Technology, Tsukuba, 305-8562, Japan. ³Department of Applied Physics, University of Tokyo, Tokyo 113-8656, Japan.

*To whom correspondence should be addressed. E-mail: s-horiuchi@aist.go.jp